Journal of Materials Chemistry A

PAPER

View Article Online
View Journal

Mn_3O_4 hollow spheres for lithium-ion batteries with high rate and capacity†

Cite this: DOI: 10.1039/c4ta00207e

Guoqiang Jian,‡[a] Yunhua Xu,‡[b] Li-Chung Lai,[c] Chunsheng Wang*[b] and Michael R. Zachariah*[ab]

Received 14th January 2014
Accepted 10th February 2014

DOI: 10.1039/c4ta00207e

www.rsc.org/MaterialsA

This work focuses on development of Mn_3O_4 hollow spheres with high cycling capacity and high rate capability in lithium ion batteries. Hollow Mn_3O_4 spheres are synthesized by an aerosol based "droplet to particle" strategy. The synthesis process involves producing and heating aerosol precursor droplets in air flow at 600 °C to induce exothermic reactions and gas blowing to form the single phase hollow Mn_3O_4 spheres. The hollow Mn_3O_4 spheres, as an anode material, deliver a highly stable cycle performance with capacity retention of ~980 mA h g^{-1} for over 140 cycles at 200 mA g^{-1} and an excellent rate capability by retaining 300 mA h g^{-1} at high current density of 10 000 mA g^{-1}.

Introduction

Rechargeable lithium ion batteries (LIBs) are a key component in portable electronics, and have become the most promising power medium in plug-in electric vehicles and integrated units for grid systems. To meet the demands from these fast growing industries, advanced electrode materials with high energy density, and good rate capability are desired to replace the current graphite-based anode materials.[1] Electrode materials for next generation LIBs should be economical to manufacture, pose minimal environmental hazard, possess high capacity, good stability and excellent rate performance.[2,3] Pioneering work by Tarascon *et al.*[4] has demonstrated that nanostructured transition metal oxides can be used as high capacity anode materials *via* a conversion reaction mechanism ($MO_x + 2xLi \leftrightarrow M + xLi_2O$). Recently, manganese and cobalt oxides have attracted attention for their high theoretical capacity and are now among the most explored metal oxide electrode materials.[5–13] Compared with cobalt oxides, manganese oxides have the advantage of nontoxicity, abundance and low cost. However, although Mn_3O_4 has a high theoretical capacity (937 mA h g^{-1}) and is isostructural with Co_3O_4, its electrochemical performance has been reported to be poor.[14,15]

Despite these earlier disappointing results, recent progress combining the designing of nanomaterials, with optimized structures, and composite components, have greatly improved the electrochemical performance of Mn_3O_4, including coating Mn_3O_4 with conductive carbon layers,[16] or forming composites with graphene or carbon nanotubes,[17–21] mesoporous Mn_3O_4 nanotubes[22] and spongelike Mn_3O_4 nanostructures.[23] The best results show capacities of ~900 mA h g^{-1} at 40 mA g^{-1} (ref. 19) and 390 mA h g^{-1} at a high current density of 1600 mA g^{-1}.[17] However, these performance improvements, come at the cost of using expensive components *i.e.* graphene based materials, or mesoporous architectures to accommodate the volume changes during lithiation/delithiation.

Use of hollow nanostructures has been proposed as an effective approach for high performance electrode materials.[24–26] The unique nature of hollow structures, including high surface area, thin walls, and hollow interior, enables electrode materials with larger electrode–electrolyte contact area, reduced diffusion path, as well as free interior space for alleviating structural strain and volume expansion.[25] Many synthetic efforts have been devoted to the fabrication of the hollow metal oxides nanostructures, however, most approaches are wet chemistry based methods.[27] Relative to wet chemistry methods, aerosol processes are usually relatively low cost, offer high purity products, and more importantly a continuous production process.[28,29] We have recently successfully fabricated hollow CuO spheres by aerosol spray pyrolysis route, useful for nanoenergetic gas generators applications.[30]

In this work, we extend this aerosol based strategy used to make hollow CuO, to fabricate hollow Mn_3O_4 spheres using a scalable aerosol "droplets to particle" route with the introduction of gas-blowing agents-sucrose and H_2O_2. In this method, the gas-blowing agents act as a gas bubbling template to form thin wall (~5–10 nm) Mn_3O_4 hollow spheres. These novel hollow Mn_3O_4 structures employed in the LIBs demonstrated high reversible capacity of ~980 mA h g^{-1} at 200 mA g^{-1} over

[a]Department of Chemistry and Biochemistry, University of Maryland, College Park, MD 20742, USA. E-mail: mrz@umd.edu

[b]Department of Chemical and Biomolecular Engineering, University of Maryland, College Park, MD 20742, USA. E-mail: cswang@umd.edu

[c]NISP Laboratory, Nanocenter, University of Maryland, College Park, MD 20742, USA

† Electronic supplementary information (ESI) available: Enlarged SAED image, SEM image and N_2 isothermal adsorption/desorption of hollow Mn_3O_4 spheres; TEM image of hollow spheres after cycling. See DOI: 10.1039/c4ta00207e

‡ These authors contributed equally to this work.

140 cycles and an excellent rate capability by retaining a capacity of 300 mA h g^{-1} at an ultra-high current density of 10 000 mA g^{-1}. To the best of our knowledge, this is the best electrochemical performance for Mn_3O_4 anode materials to date.

Experimental section

Synthesis of hollow Mn_3O_4 spheres

Hollow Mn_3O_4 spheres were synthesized by an aerosol spray pyrolysis method, as illustrated in Fig. 1. 1.00 g manganese(II) nitrate tetrahydrate ($Mn(NO_3)_2 \cdot 4H_2O$) (≥97.0%, Sigma-Aldrich), 0.171 g of sucrose ($C_{12}H_{22}O_{11}$) (Sigma-Aldrich) and 5 ml of hydrogen peroxide solution (30 wt% H_2O_2) (Sigma-Aldrich) were dissolved in 15 ml deionized water as precursor solution. Precursor solution was then atomized to form aerosol droplets by a homemade collision-type atomizer using compressed air (0.24 MPa). The geometric mean diameter of atomized formed aerosol droplets was measured to be ~1 μm using a laser aerosol spectrometer. The aerosol droplets were firstly passed through a silica-gel diffusion dryer to remove most of the water and then led to a tube furnace set at 600 °C. The normal particle residence time in the heating zone was estimated to be around 1 s. The final products of hollow Mn_3O_4 spheres were collected on a 0.4 μm HTTP filter (Millipore).

Materials characterization

The synthesized materials were characterized by transmission electron microscopy (TEM) and selected area electron diffraction (SAED) (JEOL JEM 2100F), and powder X-ray diffraction (XRD) (Bruker D8 Advance using Cu Kα radiation). After 140 cycles of charge/discharge at a current density of 200 mA g^{-1}, the electrode materials were characterized with the scanning electron microscopy (SEM, Hitachi SU 70). The thermal analysis experiment was conducted in a thermogravimetric analysis (TGA) system (SDT Q600, TA Instruments) under flow of air (100 cm^3 min^{-1}), at a heating rate of 10 °C min^{-1}. Nitrogen adsorption/desorption measurement was carried out at 77 K using an Autosorb-iQ analyzer (Quantachrome Instruments). The sample was evacuated overnight at 573 K and 1 mmHg before the measurement.

Electrochemical characterization

The hollow Mn_3O_4 spheres, carbon black and sodium carboxymethyl cellulose (CMC) binder were mixed together at the weight ratio of 70 : 15 : 15 to form a slurry and cast onto a copper foil with a loading of 0.5–1.0 mg cm^{-2} using a doctor blade, followed by an overnight drying in a vacuum oven at 100 °C. Employing a coin cell assembly, lithium foil acts as the counter electrode, 1 M $LiPF_6$ in a mixture of ethylene carbonate/diethyl carbonate (EC/DEC, 1/1 by volume) functions as the electrolyte, and Celgard®3501 (Celgard, LLC Corp., USA) as the separator. Cyclic voltammogram was recorded by a Solatron 1260/1287 Electrochemical Interface (Solartron Metrology, UK) at a scanning rate of 0.1 mV s^{-1} between 0 and 3 V. An Arbin battery test station (BT 2000, Arbin Instruments, USA) was used to test the electrochemical performance. Rate capability was examined at different current densities from 200 to 10 000 mA g^{-1}.

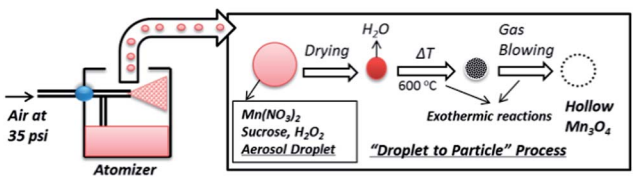

Fig. 1 Schematic formation of hollow Mn_3O_4 spheres in a "droplet to particle" aerosol spray pyrolysis process.

Results and discussion

Synthesis of hollow Mn_3O_4 spheres

The synthesis strategy of the hollow Mn_3O_4 spheres is based on an *in situ* gas blowing mechanism in single aerosol droplets, as schematically illustrated in Fig. 1. It consists of atomizing precursor solutions that contains $Mn(NO_3)_2$, sucrose, and H_2O_2, into aerosol droplets and dispersing them inside a carrier gas-air. The aerosol droplets undergo solvent (H_2O) evaporation, chemical reaction and sintering to form hollow particles. Sucrose and H_2O_2 in the precursor, act as *in situ* gas blowing agents to produce CO_2 and H_2O. Together with the inherent gas generation properties of the nitrate salt, the gas blowing agents promote the formation of hollow structure, as discussed in our recent publication.[30]

Fig. 2a shows a TEM image of the resulting Mn_3O_4 materials with a clear hollow structure and ultra-thin walls. The ring pattern selected-area electron diffraction (SAED) in Fig. 2a (Enlarged version in Fig. S1†) indicates the polycrystalline structure of the hollow Mn_3O_4 spheres. The SAED pattern show reflections corresponding to *d*-values of Mn_3O_4 phase. Some sharp reflections with *d*-values of ~0.49, 0.31, 0.25, 0.20, 0.15,

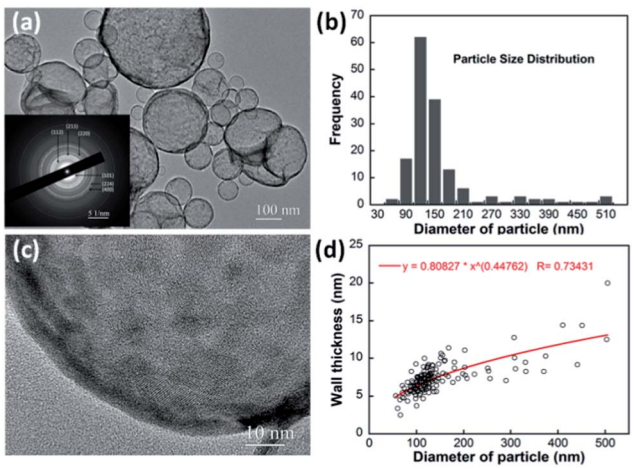

Fig. 2 (a) TEM and SAED images of as collected hollow Mn_3O_4 spheres; (b) particle size distribution of hollow Mn_3O_4 spheres based on TEM measurement; (c) high resolution TEM image of hollow Mn_3O_4 sphere; (d) the relationship of wall thickness of hollow Mn_3O_4 with particle size. Notes: the total counts are 158 in (b and d).

and 0.14 nm, represent diffraction from (101), (112), (211), (220), (224), and (400) planes of Mn_3O_4 phase (Fig. 2a).

The size distribution of as prepared hollow spheres was obtained by measuring and analyzing a total number of 158 particles in TEM images and plotted in Fig. 2b. Most particles fall in the range of ~90 to 210 nm, and the most probable particle size is ~120 nm. Compared to template-based approaches for hollow structures, the aerosol approach in this study shows a relatively wide size distribution (also see SEM image in Fig. S2†), which is typical of the size distribution from the atomization of liquids. N_2 adsorption/desorption isothermal curves (Fig. S3a†) show an obvious hysteresis loop, indicating the existence of mesopores within the sample. This is further confirmed by the pore size distribution (Fig. S3b†) which clearly shows a sharp mesopore peak around 5.6 nm. The specific surface area (calculated by BET method) of the hollow Mn_3O_4 spheres is ~96 $m^2\ g^{-1}$. High resolution TEM image in Fig. 2c shows that the spheres have ultra-thin walls with thickness of ~5 nm. The wall of the spheres in fact is actually comprised of small nanocrystals (5–10 nm) with pores, in accordance with the N_2 adsorption/desorption isothermal results. The shell thickness of 158 hollow spheres in TEM was measured individually. The relationship of shell thickness *versus* sphere particle size is shown in Fig. 2d, indicates that most particles have a shell thickness of 5–10 nm, but that wall thickness increases monotonically with the particle size. Ideally, the wall thickness should be proportional to the initial droplets size if all gases produced during chemical reactions were employed to puff the particles, as schematically shown in Fig. 3. However, this is not the case shown in Fig. 2d, where the thickness of the wall does not increase linearly with the change of particle size. Since initial droplets contain the same concentration of solutes, the amount of gas produced is directly proportional to the droplet volume. However, the amount of gas that should escape a particle during blowing should be proportional to the surface area of the particles. This leads to the result that larger droplets will lose a smaller faction of gas and this gas should result in greater expansion and thinner walls for larger particles.

Powder diffraction in Fig. 4 shows the material to be crystalline Mn_3O_4 phase (JCPDS no. 18-0803), with no observed impurities, which is in agreement with the SAED analysis. Interestingly, no phase of Mn_2O_3 was observed in the product, although Mn_2O_3 is the stable phase at 600 °C.[31] To study the

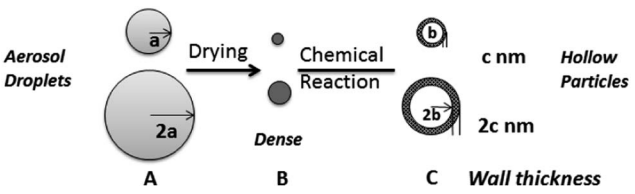

Fig. 3 The ideal relationship of wall thickness of hollow particle with initial aerosol droplet size. Note: the process is based on an ideal gas blowing assumption that all gases produced in chemical reactions are used for blowing the particles.

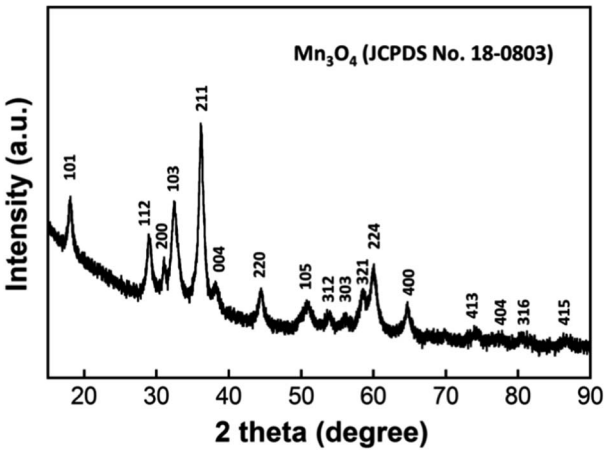

Fig. 4 X-ray diffraction pattern of hollow Mn_3O_4 spheres.

decomposition of $Mn(NO_3)_2 \cdot 4H_2O$, TGA and DSC analysis was performed in air, from room temperature to 1200 °C at a heating rate of 10 °C min^{-1}, as shown in Fig. 5. Beginning at 37 °C, we observe an endotherm with no corresponding mass change which we attribute to melting of $Mn(NO_3)_2 \cdot 4H_2O$ (m.p. = 37 °C). Three mass loss regimes are observed below 250 °C should be from endothermic dehydration, and nitrate decomposition. The overall mass loss between 15 and 250 °C amounts to ~64.4%, and is close to the 65.3% expected for the formation of MnO_2 from decomposition of $Mn(NO_3)_2 \cdot 4H_2O$. Upon further heating, further mass loss around 530 and 925 °C, are associated with two endothermic peaks, correspond to the formation of Mn_2O_3 and Mn_3O_4 respectively.[31]

We observe single phase Mn_3O_4 under our synthesis conditions at 600 °C. During synthesis, the gas generation chemistry which involves the oxidation of sucrose, is exothermic, thus it is quite possible that the actual particle temperature is higher than the reactor temperature. This suggests that the sucrose and H_2O_2 in the precursor not only act as gas blowing agents, but may also act as a fast heating source in the particle. In this context, the aerosol spray pyrolysis process in this report is

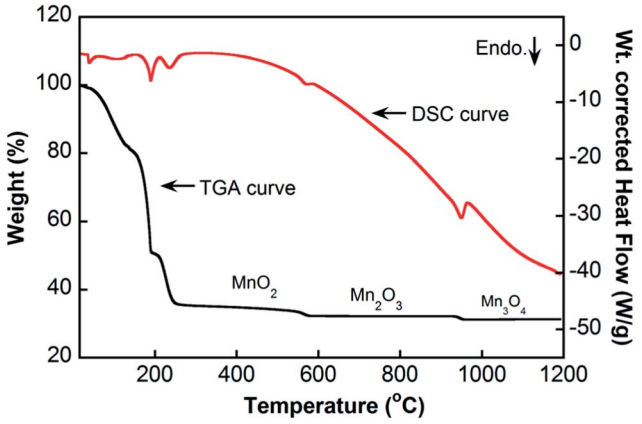

Fig. 5 TGA-DSC curves of $Mn(NO_3)_2 \cdot 4H_2O$ decomposition in air (heating rate: 10 °C min^{-1}, air flow: 100 ml cm^{-3}).

similar to the solution combustion synthesis of metal oxide nanoparticles.[32,33] In the solution combustion process for producing metal oxide nanoparticles, metal nitrate and glycine ($CH_2NH_2CO_2H$) are ignited in air, and the energy release from the combustion reaction is used to drive the formation chemistry.[33] However, the reaction in our system occurs in a more controlled manner. Firstly, a less reactive fuel – sucrose in place of glycine was used. Secondly, the organic fuel (sucrose) is confined within a single droplet, and the droplet is very fuel lean with a molar ratio of $Mn(NO_3)_2/C_{12}H_{22}O_{11} = 8$, with additional oxidizer available from ($2H_2O_2 = 2H_2O + O_2$), as well as the carrier gas (air). Under such conditions, the combustion is significantly moderated from being violent, which would shatter the droplet/particle, to a condition of a mild exothermic event resulting in gas-blowing. Nevertheless the exothermicity appears sufficient to raise the particle temperature such that Mn_3O_4 can be formed at only 600 °C (reactor temperature), rather than the nominal 925 °C from $Mn(NO_3)_2 \cdot 4H_2O$ decomposition.

Electrochemical performance

Fig. 6 shows the CV curves in the initial five scans of the hollow Mn_3O_4 electrode materials between 0.0 and 3.0 V at a scan rate of 0.1 mV s^{-1}. A broad reduction peak around 1.2 V was observed in the first scan and disappeared afterwards, which is ascribed to the decomposition of electrolyte and formation of solid-state interface films and the reduction of Mn^{3+} to Mn^{2+}. The main reduction reaction to Mn^0 occurred at 0.2 V, in the first cycle. In the following cycles, it shifted to a higher voltage of 0.3 V, which is a common to manganese oxide electrodes, and was attributed to the structure changes during the lithium insertion in the first cycle.[11] In the anodic process, the oxidation of Mn^0 to Mn^{2+} occurred at around 1.3 V, while a broad peak appears after 2 V is assigned to the further oxidation of Mn^{2+} to Mn^{3+}. The almost identical oxidation/reduction behavior from the second cycle demonstrates good reversibility, and stability of the hollow Mn_3O_4 spheres.

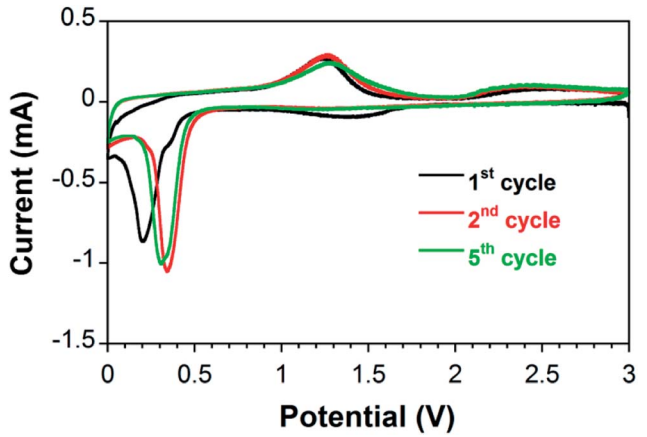

Fig. 6 Cyclic voltammograms of the 1st, 2nd and 5th cycles of hollow Mn_3O_4 spheres (scan rate 0.1 mV s^{-1}).

The charge/discharge profiles of the hollow Mn_3O_4 spheres in the first two cycles are shown in Fig. 7a. The general trend of the charge–discharge profile is consistent with previous reports on Mn_3O_4 anode materials.[17–23] It is seen from the first discharge curve that 1.6 to 0.4 V is due to the formation of solid–electrolyte interface (SEI) and the initial reduction of Mn_3O_4.[19] A well-defined voltage plateau at 0.4 V is contributed from the main lithiation reaction of Mn_3O_4 hollow spheres.[23] Similar to the CV results, the lithiation plateau moves to a higher voltage of 0.6 V in the second cycle, which implies the structure change in the first cycle lowers the lithiation resistance in the second cycle. The charge curves have two slope plateaus in the ranges of 1–1.5 V and 2.2–3.0 V, corresponding to the oxidation of Mn^0 to Mn^{2+} and Mn^{2+} to Mn^{3+},[23] respectively. In the first cycle, the discharge and charge capacities were 1066 and 1609 mA h g^{-1},

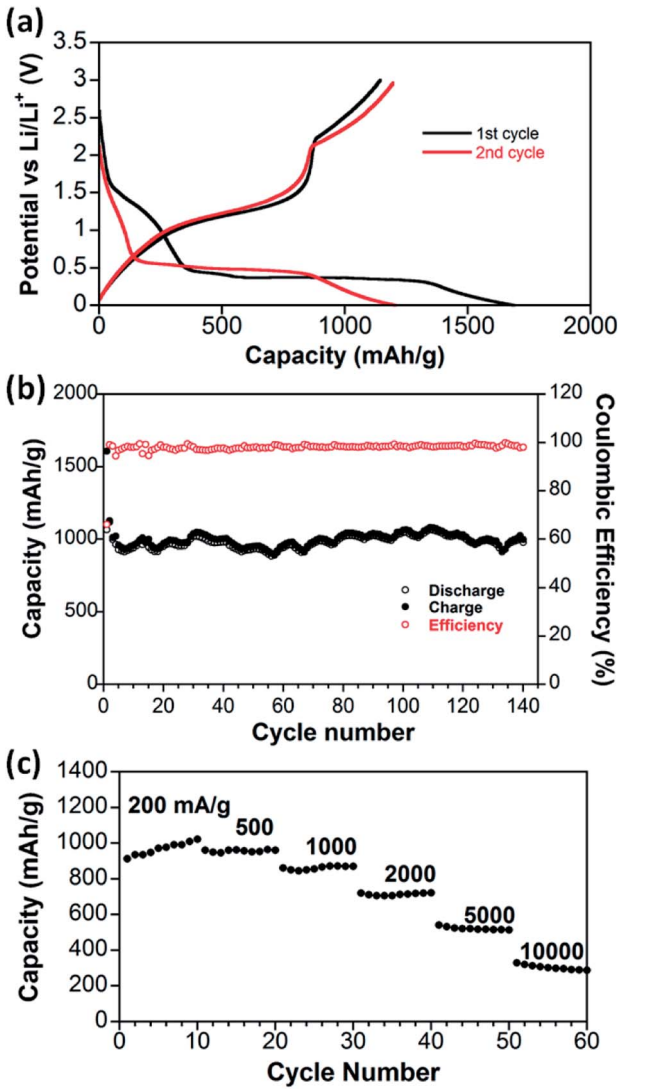

Fig. 7 Electrochemical performance of hollow Mn_3O_4 spheres as electrode materials. (a) Charge/discharge profiles for the initial two cycles at a current density of 200 mA g^{-1}; (b) cycling performance at a current density of 200 mA g^{-1}; (c) rate performance at different current densities.

respectively. The irreversible capacity in the first cycle (34%) was mainly attributed to the formation of SEI films. In the second cycle, the Coulombic efficiency is higher than 99%. The reversible capacity is around 980 mA h g^{-1}, higher than the theoretical value of 937 mA h g^{-1} for the conversion reaction: $Mn_3O_4 + 8Li^+ + 8e^- \rightarrow 3Mn(0) + 4Li_2O$. The extra capacity was also observed for other metal oxide materials and an interfacial mechanism has been proposed, in which the excess lithium was stored in the boundary regions between nanosized metal particles and Li_2O grains produced by the conversion reaction.[34,35]

The cycling stability of the hollow Mn_3O_4 spheres was examined by charging/discharging between 0.0 and 3.0 V at a current density of 200 mA g^{-1}. The cycling performance was shown in Fig. 7b. The hollow Mn_3O_4 sphere anode exhibits a superior stability with no capacity loss except the first two cycles. The capacity retention is ~980 mA h g^{-1} in the 140th cycle. The Coulumbic efficiency of the hollow Mn_3O_4 spheres approaches 100% after the second cycle, indicating a stable reversibility. This has drawn attention to the fact that the lithium ion storage of the hollow Mn_3O_4 materials in this study is superior to those Mn_3O_4 anode materials reported in the literature.[14–23] Apparently, the unique structure of thin-walled hollow structure is responsible for the improved electrochemical performances. However, while increasing the lithium ion storage capacity, the hollow structure does inevitably lead to a reduced volumetric energy density.

The rate capability of hollow Mn_3O_4 materials was evaluated at current rates of 200–10 000 mA g^{-1} (Fig. 7c). At 200 mA g^{-1}, it delivers a reversible capacity of ~950 mA h g^{-1}, which is comparable to capacity at 200 mA g^{-1}. Even at a very high rate of 5000 and 10 000 mA g^{-1}, the hollow Mn_3O_4 spheres can deliver capacities of as high as 520 and 300 mA h g^{-1}, respectively. The 300 mA h g^{-1} capacity obtained at the high current of 10 000 mA g^{-1} is still comparable to the graphite anode, one currently used in commercial batteries. Such a remarkable rate capability of the Mn_3O_4 hollow structure is superior to those with carbon coating and graphene wrapped manganese oxide anode materials,[17–21] represents the best rate performance of Mn_3O_4 anode materials. Apparently, the exceptional rate capability is benefited from the unique thin wall hollow structure, which provides a significantly reduced path for both electron and ion diffusion.[25]

As mentioned above, the unique structure of the hollow Mn_3O_4 spheres is responsible for the good cycling performance and rate capability. The morphology of the hollow Mn_3O_4 spheres after 140 cycles was investigated with SEM (Fig. 8) and TEM (Fig. S4†). Compared with the TEM image (Fig. 1) and SEM image (Fig. S2†), the SEM image of the cycled electrodes show no obvious morphology changes, demonstrating a robust structure of the hollow spheres, which can effectively alleviate the structural strain and accommodate the large volume change during repeated lithiation/delithiation. TEM image (Fig. S4†) of hollow spheres after cycling show no obvious change regarding the wall thickness compared with the as synthesized hollow spheres (Fig. 1).

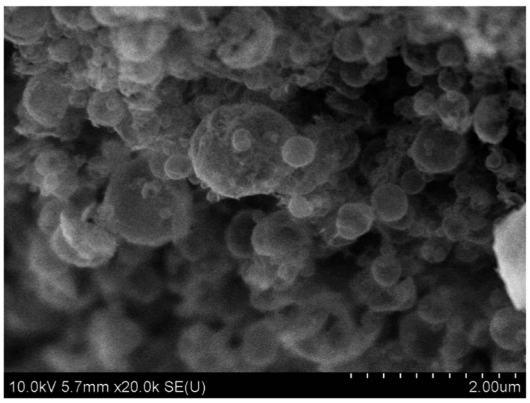

Fig. 8 SEM image of hollow Mn_3O_4 spheres after 140 cycles at a current density of 200 mA g^{-1}.

Conclusion

In summary, this work reports hollow Mn_3O_4 spheres with an ultra-thin shell which demonstrates superior electrochemical performance as anode materials in lithium-ion batteries than any previously reported in the literature. The hollow Mn_3O_4 spheres exhibited good stability, with high capacity retention of ~980 mA h g^{-1} over 140 cycles, and exceptional rate capability. The outstanding electrochemical performance is attributed to its unique structure, of a hollow interior and ultra-thin wall.

Acknowledgements

The authors would like to thank the funding support from the Army Research Office. We acknowledge the support of Maryland Nanocenter and its NispLab. The NispLab is supported in part by the NSF as a MRSEC Shared Experimental Facility. The authors are also thankful to Dr Dongxia Liu and Yiqing Wu for assistance with N_2 isotherm measurement of the sample.

Notes and references

1 B. Dunn, H. Kamath and J.-M. Tarascon, *Science*, 2011, **334**, 928–935.
2 N. S. Choi, Z. H. Chen, S. A. Freunberger, X. L. Ji, Y. K. Sun, K. Amine, G. Yushin, L. F. Nazar, J. Cho and P. G. Bruce, *Angew. Chem., Int. Ed.*, 2012, **51**, 2–33.
3 M. G. Kim and J. Cho, *Adv. Funct. Mater.*, 2009, **19**, 1497–1514.
4 P. Poizot, S. Laruelle, S. Grugeon, L. Dupont and J.-M. Tarascon, *Nature*, 2000, **407**, 496–499.
5 M. V. Reddy, G. V. Subba Rao and B. V. R. Chowdari, *Chem. Rev.*, 2013, **113**, 5364–5457.
6 X. W. Lou, D. Deng, J. Y. Lee, J. Feng and L. A. Archer, *Adv. Mater.*, 2008, **20**, 258–262.
7 Y. G. Li, B. Tan and Y. Y. Wu, *Nano Lett.*, 2008, **8**, 265–270.
8 X. Y. Yang, K. C. Fan, Y. H. Zhu, J. H. Shen, X. Jiang, P. Zhao, S. R. Luan and C. Z. Li, *ACS Appl. Mater. Interfaces*, 2013, **5**, 997–1002.

9 W. Luo, X. L. Hu, Y. M. Sun and Y. H. Huang, *ACS Appl. Mater. Interfaces*, 2013, **5**, 1997–2003.
10 S. Nayak, S. Malik, S. Indris, J. Reedijk and A. K. Powell, *Chem. – Eur. J.*, 2010, **16**, 1158–1162.
11 J. C. Guo, Q. Liu, C. S. Wang and M. R. Zachariah, *Adv. Funct. Mater.*, 2012, **22**, 803–811.
12 H. Xia, M. O. Lai and L. Lu, *J. Mater. Chem.*, 2010, **20**, 6896–6902.
13 C. Chae, J. H. Kim, J. M. Kim, Y. K. Sun and J. K. Lee, *J. Mater. Chem.*, 2012, **22**, 17870–17877.
14 D. Pasero, N. Reeves and A. R. West, *J. Power Sources*, 2005, **141**, 156–158.
15 Q. Fan and M. S. Whittingham, *Electrochem. Solid-State Lett.*, 2007, **10**, A48–A51.
16 C. B. Wang, L. W. Yin, D. Xiang and Y. X. Qi, *ACS Appl. Mater. Interfaces*, 2012, **4**, 1636–1642.
17 H. L. Wang, L. F. Cui, Y. Yang, H. S. Casalongue, J. T. Robinson, Y. Y. Liang, Y. Cui and H. J. Dai, *J. Am. Chem. Soc.*, 2010, **132**, 13978–13980.
18 S. Y. Liu, J. Xie, Y. X. Zheng, G. S. Cao, T. J. Zhu and X. B. Zhao, *Electrochim. Acta*, 2012, **66**, 271–278.
19 L. Li, Z. P. Guo, A. J. Du and H. K. Liu, *J. Mater. Chem.*, 2012, **22**, 3600–3605.
20 N. Lavoie, P. R. L. Malenfant, F. M. Courtel, Y. Abu-Lebdeh and I. J. Davidson, *J. Power Sources*, 2012, **213**, 249–254.
21 Z. H. Wang, L. X. Yuan, Q. G. Shao, F. Huang and Y. H. Huang, *Mater. Lett.*, 2012, **80**, 110–113.
22 Z. C. Bai, N. Fan, Z. C. Ju, C. L. Guo, Y. T. Qian, B. Tang and S. L. Xiong, *J. Mater. Chem. A*, 2013, **1**, 10985–10990.
23 J. Gao, M. A. Lowe and H. D. Abruna, *Chem. Mater.*, 2011, **23**, 3223–3227.
24 X. W. Lou, L. A. Archer and Z. C. Yang, *Adv. Mater.*, 2008, **20**, 3987–4019.
25 Z. Y. Wang, L. Zhou and X. W. Lou, *Adv. Mater.*, 2012, **24**, 1903–1911.
26 X. Y. Lai, J. E. Halpert and D. Wang, *Energy Environ. Sci.*, 2012, **5**, 5604–5618.
27 J. Hu, M. Chen, X. S. Fang and L. M. Wu, *Chem. Soc. Rev.*, 2011, **40**, 5472–5491.
28 K. Okuyama and I. W. Lenggoro, *Chem. Eng. Sci.*, 2003, **58**, 537–547.
29 C. Boissiere, D. Grosso and A. Chaumonnot, *Adv. Mater.*, 2011, **23**, 599–623.
30 G. Q. Jian, L. Liu and M. R. Zachariah, *Adv. Funct. Mater.*, 2013, **23**, 1341–1346.
31 E. R. Stobbe, B. A. d. Boer and J. W. Geus, *Catal. Today*, 1999, **47**, 161–167.
32 L. A. Chick, L. R. Pederson, G. D. Maupin, J. L. Bates, L. E. Thomas and G. J. Exarhos, *Mater. Lett.*, 1990, **10**, 6–12.
33 A. S. Mukasyan, P. Epstein and P. Dinka, *Proc. Combust. Inst.*, 2007, **31**, 1789–1795.
34 J. Maier, *Solid State Ionics*, 2002, **148**, 367–374.
35 P. Balaya, H. Li, L. Kienle and J. Maier, *Adv. Funct. Mater.*, 2003, **13**, 621–625.

